Full Length Article

Combinatorial study of the structural, optical, and electrical properties of low temperature deposited $Cd_{1-x}Zn_xTe$ $(0 \leq x \leq 1)$ thin films by MOCVD

G. Kartopu [*], Q. Fan, O. Oklobia, S.J.C. Irvine

Centre for Solar Energy Research, OpTIC, St. Asaph Business Park, St. Asaph LL17 0JD, UK

ARTICLE INFO

ABSTRACT

Polycrystalline $Cd_{1-x}Zn_xTe$ thin films prepared by a combinatorial MOCVD process were characterised for their structural, optical, and electrical properties. Films became smoother with smaller grains displaying higher sub-bandgap transmittance with increasing x. The X-ray diffraction pattern indicated (1 1 1) texture for all films, with increasing compositional inhomogeneity for ternary compositions. Room-temperature optical transmittance and micro-photoluminescence (PL) spectra were analysed to determine the dependence of composition with the bandgap. The non-linear variation of the bandgap with composition was fitted, giving around 0.7 and 0.3 band bowing parameters from optical and PL spectra, respectively. Raman scattering experiments showed that ZnTe-like LO mode varies linearly for $x > 0.2$. However, Te-related modes (due to surface migration of tellurium) emerge along with the smearing out of parent Raman modes with increasing excitation power. Temporal behaviour of Te modes with excitation power indicated formation of tensile stress due to laser heating. The film resistance increased up to 4 orders of magnitude, corroborating with the semiconductor grain size trend, with increasing Zn concentration. Post-growth annealing of the films in a hydrogen environment above 430 °C decreased the inhomogeneity in ternary alloys, making these films more appealing, for example, for photovoltaic applications.

1. Introduction

Tandem photovoltaic (PV) solar cells have recently become a hot topic of study. This is motivated by the stagnating solar-to-electricity conversion efficiency of crystalline silicon (c-Si) cells, which have the highest share (around 90%) in the solar PV market. To overcome this performance limitation, a suitable thin film PV technology (to operate with a c-Si rear cell) is needed which can effectively harvest the short wavelength photons in the solar spectrum. The c-Si rear cell is expected to utilize photons in the near infrared range, which are transmitted through the thin film top cell. Other requirements for the top cell are low manufacturing cost and high stability (ideally 25 years, matching the lifetime of c-Si cells). Several thin film candidates have been considered for tandem application with c-Si. The most studied ones are the Perovskite [1,2] and epitaxial III-V [3,4] thin film cells. High tandem performance was observed using either of these top cells [5,6]. However, at present these candidates appear unsuitable for manufacturing, as they lack either the stability or the cost-efficiency, and hence require further development.

The polycrystalline CdTe thin film technology is the runner-up in the solar market with around 5% share and hence may offer a natural alternative. However, to obtain the highest performance with a c-Si rear cell, the bandgap of CdTe should be expanded towards 1.8 eV [7]. This can be achieved by alloying the CdTe absorber with, e.g. Zn or Mg. $Cd_{1-x}Zn_xTe$ alloy crystals having a low Zn content (up to 20%) in particular have been studied extensively for radiation (gamma and X-ray) detectors [8], due to their higher electrical resistance and lower defect density compared to pure CdTe. A small number of reports investigated the full range of $Cd_{1-x}Zn_xTe$ compositions. For example, epitaxial $Cd_{1-x}Zn_xTe$ films grown on GaAs (0 0 1) substrates by molecular beam epitaxy were characterised by Raman spectroscopy [9] and optical spectroscopy [10]. Kosyak et al. deposited thick polycrystalline $Cd_{1-x}Zn_xTe$ films by close spaced vacuum sublimation on glass substrates and studied their photoluminescence and structural properties [11]. More recently, Moger et al. grew polycrystalline $Cd_{1-x}Zn_xTe$ thin films by a vacuum co-evaporation method and measured their optical, structural, and electrical properties [12]. However, no detailed study was published on the preparation and properties of polycrystalline

Cd$_{1-x}$Zn$_x$Te thin films by the metalorganic chemical vapor deposition (MOCVD) method. MOCVD can be a powerful method for semiconductor thin film growth, allowing control with alloy composition, film crystallinity, doping and physical properties [13].

In this paper, we prepared a full library of polycrystalline Cd$_{1-x}$Zn$_x$Te thin film compositions ($0 \leq x \leq 1$) using a combinatorial MOCVD process and studied their physical properties by an extensive range of techniques, in scope for tandem PV applications.

2. Experimental details

Thin film samples (2 μm thickness) were deposited on 5×5 cm^2 borosilicate glass substrates in a horizontal MOCVD reactor at 360 °C. A 1×1 cm^2 indium tin oxide (ITO) coated borosilicate glass with 4–8 Ω/□ sheet resistance was also present in each run for electrical characterisation of the films. Metalorganic precursors dimethylcadmium (DMCd), diethylzinc (DEZn), and diisopropyltelluride (DiPTe) were carried and then further diluted by high-purity hydrogen at total flow rate of 4 l/min. The DMCd/(DeZn + DMCd) ratio was varied between 0 and 1 to alter the film composition. Due to the horizontal geometry of the reactor, depletion of DMCd precursor was observed along the flow direction, which caused downstream enrichment of Zn in the ternary films (see illustration in Fig. S1). The lateral variation in Cd$_{1-x}$Zn$_x$Te composition enabled a rapid combinatorial analysis, towards forming a library on the composition dependence of film properties. The coated borosilicate substrates were cleaved into 1×1 cm^2 pieces, providing access to ranges of Cd$_{1-x}$Zn$_x$Te compositions. The total number of growth runs was thereby limited to 5; CdTe, ZnTe, and 3 Cd$_{1-x}$Zn$_x$Te. The value of x was determined by energy dispersive spectroscopy (EDS) via the atomic ratio $x = $ Zn/(Zn + Cd). Selected films were also annealed in flowing H$_2$ for 10 min at temperatures ranging from 400 to 520 °C (30 °C step size), to assess effects on film structure towards solar cell applications. No surface treatment was applied to any of the thin films characterized in this work.

The EDS analysis and scanning electron microscopy (SEM) characterisation of the films were carried out using a Hitachi TM3000 table-top SEM with an EDS detector (Oxford Instruments). Micro-Raman and PL measurements were performed at room temperature with a Renishaw inVia confocal Raman microscope (Renishaw plc., Wotton-Under-Edge, UK) in the backscattering configuration using 532 nm laser operated at a maximum power of 30 mW with a 50x objective (numerical aperture = 0.50, beam diameter ≈ 1 μm). X-ray diffraction (XRD) measurements were obtained using a D8 Discover instrument (Bruker, Karlsruhe, Germany) diffractometer in the θ–2θ configuration with a Cu-Kα source ($\lambda = 0.15418$ nm) operated at 40 kV and 40 mA.

A Keithley 617 electrometer in a microprocessor-controlled measuring system was used for steady state electrical (current–voltage, I-V) measurements of thin films sandwiched between ITO (bottom) and gold (top) electrodes at room temperature. The gold pads were vacuum evaporated and had 1 mm diameter. Gold was chosen since its high work function (5.1 eV) is expected to provide an Ohmic-like contact to the Cd$_{1-x}$Zn$_x$Te. The samples were contained under high vacuum conditions of $< 10^{-6}$ Torr in an Oxford Instruments cryostat to control the ambient temperature. During measurements, slight transient current variation occurred when the voltage was applied; time was allowed for this to stabilize before readings were taken. The applied voltage was swept from −5 V to 5 V to collect the I-V data. The light measurements were carried out with the illumination provided by a 405 nm laser operated at power density of 0.051 mW/mm^2.

3. Results

3.1. Structural properties

SEM micrographs of selected films are given in Fig. 1. The grains in the CdTe film are relatively large, faceted and range from about 0.5 to 1 μm in diameter. The grain size monotonically decreased with increasing value of x. The Zn-rich films and ZnTe appeared smoother, presenting smaller grains down to 0.1 μm in size.

The XRD pattern of thin films mainly depends on the composition, preparation process and substrate materials. XRD patterns of selected films are given in Fig. 2. All samples showed polycrystalline characteristics (expected due to the non-lattice matching substrate) with a 111-texture of the cubic structure, consistent with JCPDS data files
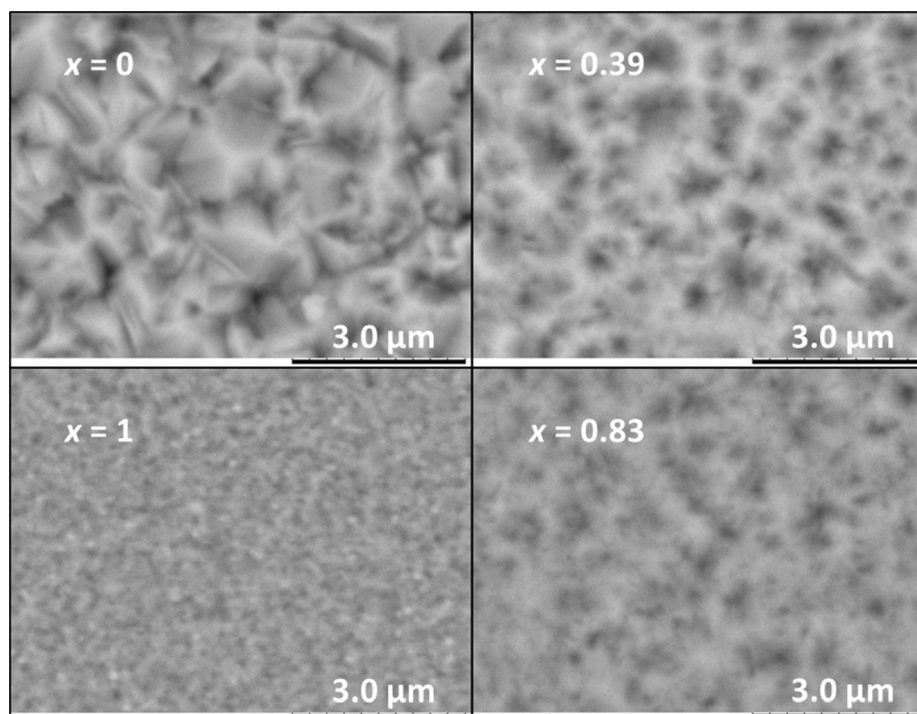

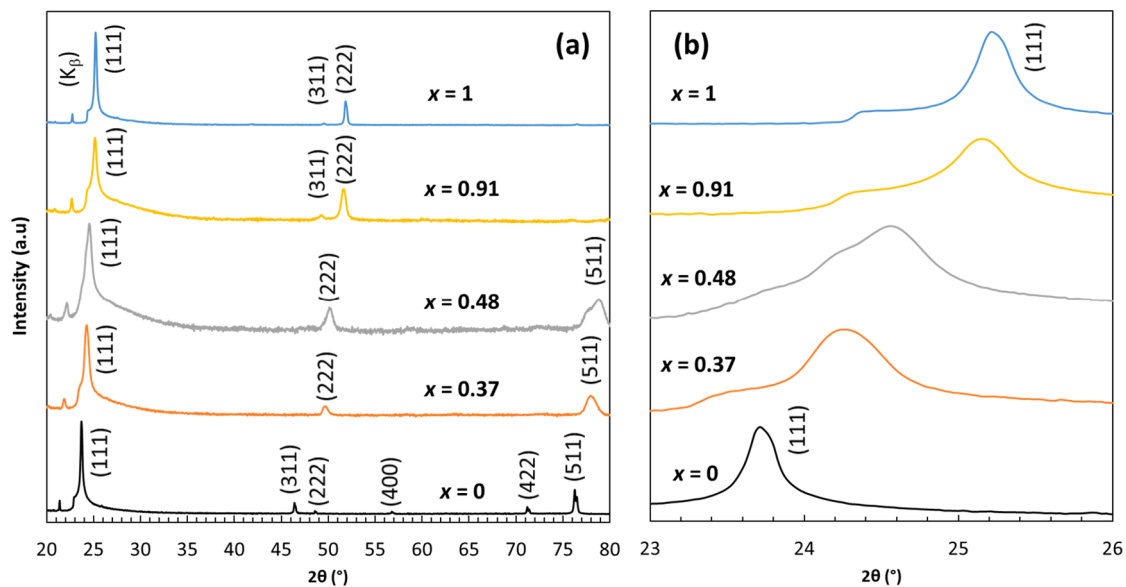**Fig. 1.** Plan-view (SEM) of selected Cd$_{1-x}$Zn$_x$Te thin films.

Fig. 2. XRD spectrum of selected $Cd_{1-x}Zn_xTe$ samples: (a) wide range view and (b) expanded view around the dominant (111) peak.

01–089-3054 for ZnTe, 015–0770 for CdTe, and 050–1440 for $Cd_{1-x}Zn_xTe$. The (111) peak is positioned at $2\theta = 23.74°$ for CdTe and $25.24°$ for ZnTe and ranged in between these values for the ternary alloys. According to Vegard rule, the diffraction peaks shift to higher 2θ values with increasing Zn concentration since atomic radius of Cd (158 pm) is greater than that of Zn (139 pm). For the CdTe film, other diffraction peaks were at $46.50°$ (311), $49.51°$ (222), $56.8°$ (400), $71.6°$ (422), and $76.2°$ (511).

For the binary films (CdTe, ZnTe) the (111) reflection appeared relatively narrow (Table 1). Local compositional fluctuations and/or higher crystal disorder may be at play, leading to broader peaks, for the ternary films. We note the (111) peak width did not follow the trend of SEM grain sizes with composition. Thus, the wider XRD peaks of the $Cd_{1-x}Zn_xTe$ ternary film can be attributed to crystal disorder and local compositional inhomogeneity rather than e.g. finite crystallite size, which ranges from 30 to 70 nm for these samples as estimated via the Scherrer equation. In particular, a shoulder to main (111) peak of the $x = 0.48$ sample indicates co-existence of two different $Cd_{1-x}Zn_xTe$ compositions. Splitting of the main (111) peak was also reported for thermally evaporated $Cd_{1-x}Zn_xTe$ alloy films (for $0.8 < x < 0.6$ range) which was attributed to the co-existence of cubic and hexagonal phases [12]. We attribute the peak broadening and local inhomogeneity to spinodal decomposition which will be discussed below.

From the XRD data, the lattice constant (*a*) was calculated via the (111) main peak according to Bragg's law [$n \lambda = 2 \times d \times \sin\theta$], where $d (hkl) = a / (h^2 + k^2 + l^2)^{1/2}$. In Table 1, we also compare the film composition calculated by Vegard rule with the EDS data. A good agreement can be seen between these results with the highest variance of around 6%.

3.2. Optical properties

The film appearance changed from dark black for CdTe to greyish black for the relatively low *x* films; ZnTe was orange like while the Zn-rich films appeared grey with a hint of orange (Fig. 3a). The transmittance spectrum of the corresponding layers (Fig. 3b) revealed a steady decrease of the absorption edge, from $\sim$ 850 nm to $\sim$ 550 nm with *x* increasing from 0 to 1. Concurrently, the sub-bandgap transmittance increased with *x*; while the transmittance is about 50% for ZnTe at 900 nm, it drops to several % for CdTe. This effect can be attributed to sub-bandgap free-carrier or defect absorption as well as increased light scattering with the grains becoming larger and pyramidal towards CdTe. Further measurements on defect characterisation and light scattering would be needed to elucidate this effect. The Tauc plot of these specimens is given in Fig. 3c. A linear fit made to each curve was extrapolated to the energy axis to determine the value of bandgap (E_g). The E_g - *x* relationship (Fig. 3d) was non-linear and fitted with a second-order polynomial to yield the band bowing parameter (*b*). From this process, we obtain $b = 0.7$ for our $Cd_{1-x}Zn_xTe$ films.

Fig. 4a shows the micro-PL spectra of selected films obtained using a laser power density of 3.82×10^4 W/cm^2, except for ZnTe for which it was 1.91×10^5 W/cm^2. At lower excitation power densities, PL signal was weak for ZnTe. The ZnTe and Zn-rich ($x > 0.8$) ternary films exhibited what appeared to be a Raman spectrum with multiple phonon modes, superimposed on the PL spectra. This is believed to be due to resonance of the excitation energy with the material band gap. A similar phenomenon was reported in literature [14,15]. The PL peak energy of CdTe and ZnTe at 1.52 and 2.21 eV are very close to E_g determined by the Tauc plot (1.49 and 2.19 eV, respectively), which provide a reference to the bandgap energy estimated by the micro-PL method. Compositional dependence of the bandgap values determined by PL and transmittance methods will be discussed below. In Fig. 4b, the E_g (PL) - *x* relationship is plotted where the composition was determined by EDS. Again, using a second-order polynomial fit, we obtained the following relationship (Eqn 1), which relates the E_g (PL) to the Zn content:

$$E_g(Cd_{1-x}Zn_xTe) = 1.52 + 0.39x + bx^2 \tag{1}$$

where $b = 0.31$ is the deduced fitting (band bowing) parameter.

This suggests that micro-PL spectroscopy can be used as a complimentary technique for determining the composition of the $Cd_{1-x}Zn_xTe$ ternary alloy.

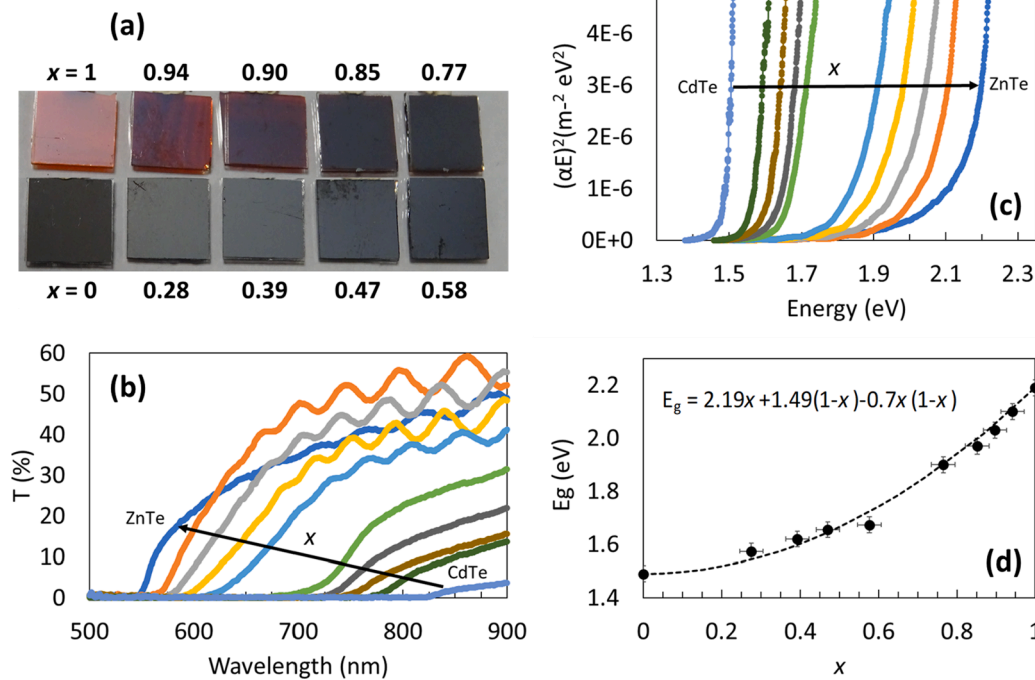Micro-Raman spectra of the thin films (also measured by micro-PL)

Table 1
XRD parameters derived using the (111) peak for the spectra shown in Fig. 2. The film composition calculated using the lattice constant is in good agreement with EDS results. Crystallite sizes (*d*) were estimated using the Scherrer equation.

Sample	(111) 2θ (°)	*a* (Å)	*x* (from XRD)	*x* (from EDS)	(111) peak FWHM (°)	*d* (nm)
CdTe	23.74	6.48	0	0	0.118	71.9
CZT1	25.18	6.16	0.96	0.91	0.266	31.2
CZT2	24.56	6.30	0.56	0.48	0.207	40.0
CZT3	24.28	6.37	0.37	0.37	0.177	46.8
ZnTe	25.24	6.10	1	1	0.148	56.1

Fig. 3. (a) Optical images and (b) transmittance of selected $Cd_{1-x}Zn_xTe$ samples. (c) Tauc plot and (d) bandgap (E_g) vs EDS composition (x) relationship derived using the transmittance spectra in (b).

collected using a power density of 3.82×10^4 W/cm² and 100 s acquisition time are displayed in Fig. 5. For CdTe, three distinct peaks at 123.1, 140.6, 163.9 cm^{-1} and a weak one at 328.8 cm^{-1} can be seen. The peak at 123.1 cm^{-1}, being very close to a Te phonon mode with A_1 symmetry reported for pure tellurium (121.5 cm^{-1}) [16], is designated as A_1 (Te), and attributed to surface Te. It is slightly blue-shifted by 1.6 cm^{-1} from that in pure Te, suggesting surface Te of the CdTe is under some compressive stress [17]. The peak labelled E (Te)/TO (CdTe) at 140.6 cm^{-1} is a superposition of E symmetry mode (141 cm^{-1}) of Te and TO mode of CdTe [16]. The third main peak at 163.9 cm^{-1} is assigned to the LO mode of CdTe [18], whilst the weaker feature at 328.8 cm^{-1} is believed to be the second order of the LO (CdTe) mode. The A_1 (Te) and E (Te)/TO (CdTe) modes are also present in the spectrum of ternary films and only slightly blueshift with increasing x (i.e. with reference to their positions in CdTe). For ZnTe, these modes are absent but LO (ZnTe) mode (205 cm^{-1}), with overtones up to the 5th order can be observed [19].

In the $x = 0.27$ Raman spectrum, the peak at 183.2 cm^{-1} is ascribed to ZnTe-like LO mode and the additional weak one at 366.7 cm^{-1} to its second order [20]. For the $x = 0.55$ film, the 1st and 2nd orders of the ZnTe-like LO mode can be seen at 191 and 378 cm^{-1}, respectively. For the most Zn-rich ternary film ($x = 0.84$), these LO (ZnTe) modes further blue-shifted to 200 and 400.6 cm^{-1}, respectively, with overtones up to the 5th order also visible, due to near resonant excitation condition (as explained above). The frequency and phonon mode assignment of all the distinct peaks observed in our $Cd_{1-x}Zn_xTe$ samples are provided in Table 2.

In Fig. 5b, the CdTe and ZnTe-like LO modes for ternary films are noted to shift to higher frequencies with increasing Zn content (x). A plot showing the compositional dependence of the first order LO modes is shown in Fig. 6. For the LO (CdTe) mode, the shift with composition appears not to be significant (varies only by 7 cm^{-1} with × increasing from 0 to 0.84) and the peak is not well resolved for all compositions. The reason this mode appears clearly for the $x = 0.84$ spectrum (but not for lower values of x) is the resonant excitation condition observed similarly to ZnTe. On the other hand, the compositional dependence of the LO (ZnTe) mode is stronger and, in general, consistent with those

reported for $Cd_{1-x}Zn_xTe$ samples prepared by CSVS, Bridgeman, PLD and MBE methods [20,21,22,9]. However, the measured frequencies of the LO (ZnTe) mode in the present work are slightly lower in comparison (Fig. 6). This could be attributed to differences in measurement conditions such as excitation parameters and measurement temperature. A single excitation wavelength (532 nm) was used for all our samples, whereas other reports employed different excitation wavelengths and powers for various values of x (to achieve better spectral resolution) [20,22]. Under resonant conditions, the high signal-to-noise ratio of the Raman spectra can be achieved with well resolved phonon mode peaks [21]; however, phonon frequencies can also shift slightly, depending on the power density used [23]. Further, our Raman spectra were collected at 300 K, in contrast to 20–80 K employed by others [21,22,24]. At low temperatures, shrinkage of the cell volume (and bond lengths) due to compressive stress leads to the blueshift of Raman frequencies. Laser heating related effects observed, such as Te surface enrichment [25], will be discussed below.

3.3. Electrical properties

Fig. 7 shows the selected I-V curves of our polycrystalline films with the Au/$Cd_{1-x}Zn_xTe$/ITO sandwich structure, as measured in dark and light conditions. Energy band diagram for CdTe, ZnTe, and the electrode materials, Au and ITO are given in Fig. S2. Due to our $Cd_{1-x}Zn_xTe$ thin films being unintentionally doped, the doping concentration and hence the position of the Fermi level (E_F) and the magnitude of work functions (ϕ) are unknown. However, assuming $Cd_{1-x}Zn_xTe$ is low p-type doped (due to residual arsenic in our MOCVD system) and so the E_F is close to the valence band, the semiconductor work function is comparable but greater than that of Au ($\phi = 5.3$ eV) and much higher than that of ITO ($\phi = 4.0$ eV). Thus, an Ohmic-like contact of low barrier height with Au and a Schottky-type contact of high barrier height with ITO are expected to form. In other words, considering the work function of the materials involved, Au/$Cd_{1-x}Zn_xTe$/ITO sandwich can be expected to have the I-V characteristic curve of two diodes in series. When $x = 0$, the CdTe film has relatively low resistance with high current. The asymmetry of positive and negative voltage of the I-V curve results from the different
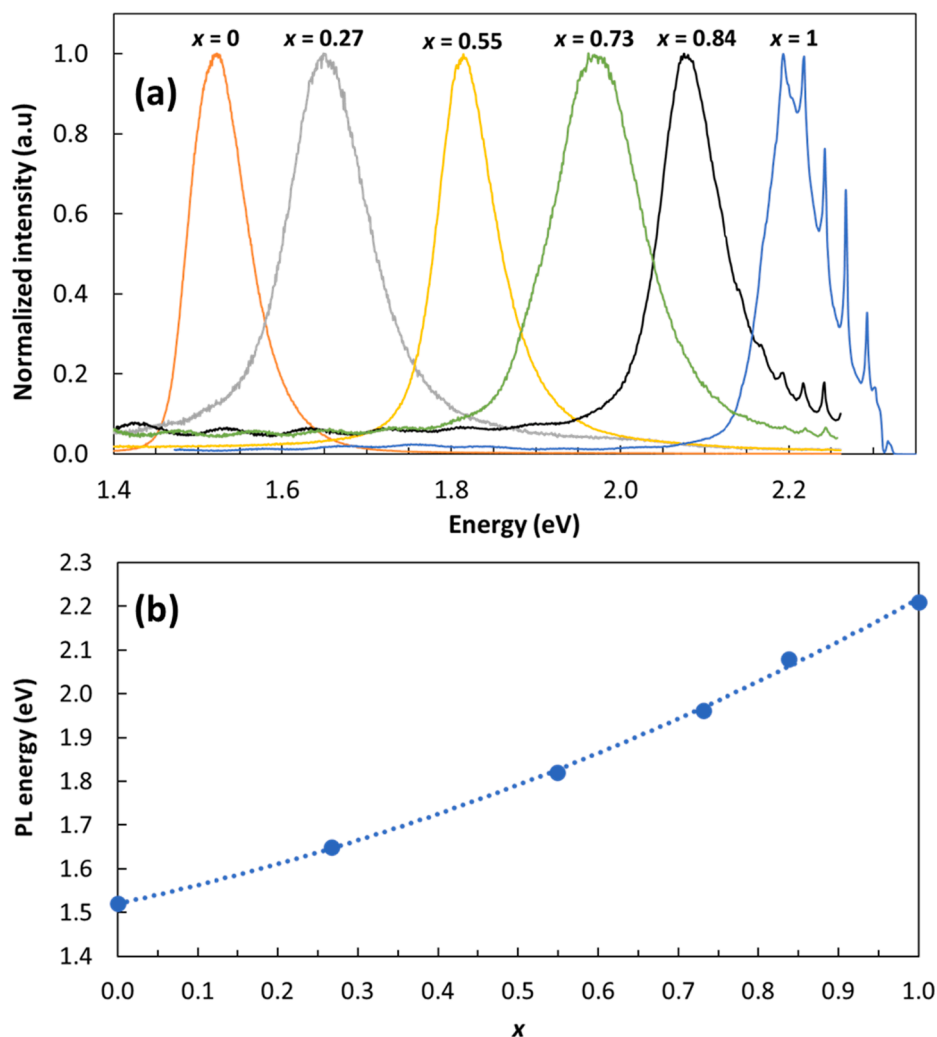
Fig. 4. (a) Micro-PL spectrum of selected $Cd_{1-x}Zn_xTe$ thin films with x = 0 (CdTe), 0.27, 0.55, 0.73, 0.84 and 1 (ZnTe), and (b) PL energy vs. composition (x).
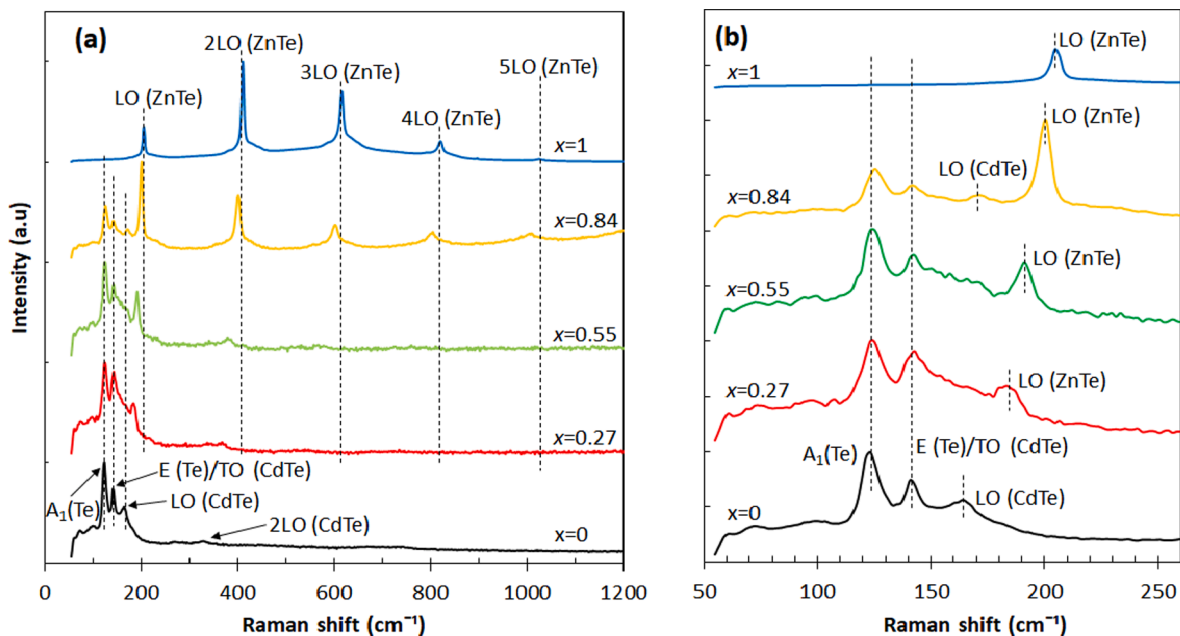

Fig. 5. Micro-Raman spectrum of selected $Cd_{1-x}Zn_xTe$ thin films: (a) wide range view and (b) expanded view of the first order Raman peaks.

Table 2

Raman mode frequencies of $Cd_{1-x}Zn_xTe$ films and corresponding phonon assignments.

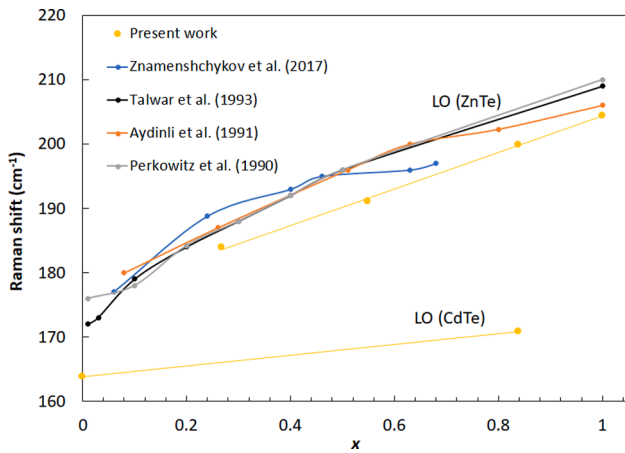| Sample	Frequency (cm^{-1})								
	A1 (Te)	E (Te)/	CdTe-like		ZnTe-like				
		TO (CdTe)	LO	2LO	LO	2LO	3LO	4LO	5LO
CdTe	123.1	140.6	163.9	328.8	–	–	–	–	–
$x = 0.27$	123.1	142.5	–	–	183.9	366.7	–	–	–
$x = 0.55$	123.1	142.5	–	–	191.1	378.0	–	–	–
$x = 0.84$	125.0	142.5	170.9	–	199.9	400.6	601.2	804.0	1008.5
ZnTe	–	–	–	–	204.4	410.0	615.9	820.0	1024.2

Fig. 6. Variation of the LO (ZnTe) and LO (CdTe) Raman frequencies as function of the $Cd_{1-x}Zn_xTe$ composition. Linear fit to our data points is drawn as a guide to the eye.

contact barrier of Au/CdTe and ITO/CdTe interfaces. High ITO/CdTe barrier leads to reverse current saturation. When $x = 0.38$, the film resistance begins to rise, and the high reverse ITO/$Cd_{1-x}Zn_xTe$ barrier leads to the saturation of reverse current. When $x = 0.82$ and $x = 1$, the electrical properties are dominated by high resistance of these materials.

Fig. 7 suggests that indeed two diodes are series connected and conform to the traditional diode I-V curve. The current is composed of a reverse leakage current, generation recombination current, diffusion current and injection current, and follows Schottky's law [26]. As can be seen, the higher the Zn content the higher the film resistance, and
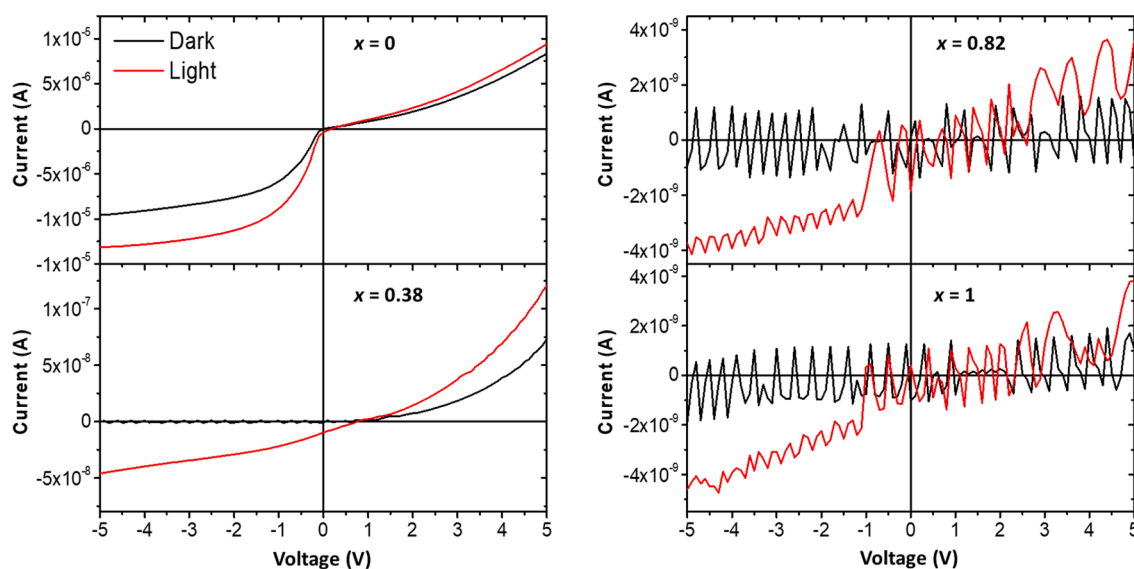
consequently the lower the measured current. We note that the lowest currents measured for Zn rich ternary and ZnTe films are close to the lower detection limit of the test system used, and thus the background noise of the test system is superimposed onto the current signal of $Cd_{1-x}Zn_xTe$, making it look noisy. In the forward current regime, there is the photo-current and generation recombination current, and the forward light current for all samples is greater than their corresponding dark values (indicating light sensitivity of the semiconductor materials). The reverse leakage current under illumination is also greater than that in dark condition. The film resistivity was estimated from the pseudo-linear part of the I-V curve in the forward regime, close to the origin, that is before the contact effect dominates (Fig. 8). For CdTe ($x = 0$), the resistivity is relatively low at $\sim 5 \times 10^7\ \Omega \cdot cm$; it increases to $\sim 4 \times 10^9\ \Omega \cdot cm$ at $x \approx 0.38$ and saturates in the region of 10^{11}-$10^{12}\ \Omega \cdot cm$ for Zn rich layers ($x \geq 0.82$). The electrical resistivity results are commensurate with the decreasing grain size observed with increasing x (Fig. 1).

3.4. Effect of annealing

Annealing treatment can have a great influence on the crystal enlargement, crystal quality and dislocation density of a polycrystalline thin film, eliminate internal stress, remove chemical residues of a low-temperature preparation process, increase film density and reduce the porosity. Fig. 9 shows the change of the half peak width (FWHM) for the (1 1 1) XRD reflection of the $Cd_{1-x}Zn_xTe$ films annealed at different temperatures. After annealing, in general, the FWHM of the (1 1 1) peak reduces for all films. For the ternary sample $x = 0.41$ the drop starts at 430 °C and continues linearly towards 520 °C. For binary films ZnTe and CdTe, however, the FWHM reduces only in the 400 to 430 °C range, beyond which it remains constant. The peak width for the ternary film approaches to that of the binary films at around 520 °C, indicating improved material uniformity. These suggest that the micro-
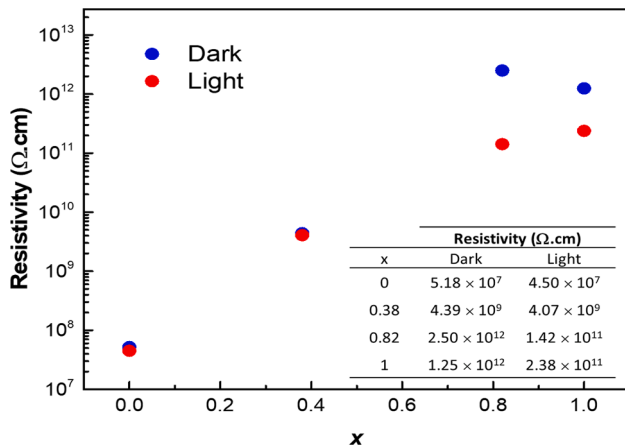

Fig. 7. Dark and illuminated I-V curves of Au/$Cd_{1-x}Zn_xTe$/ITO sandwich structure.

Fig. 8. Calculated resistivities (in the dark and light) as a function of the $Cd_{1-x}Zn_xTe$ composition.

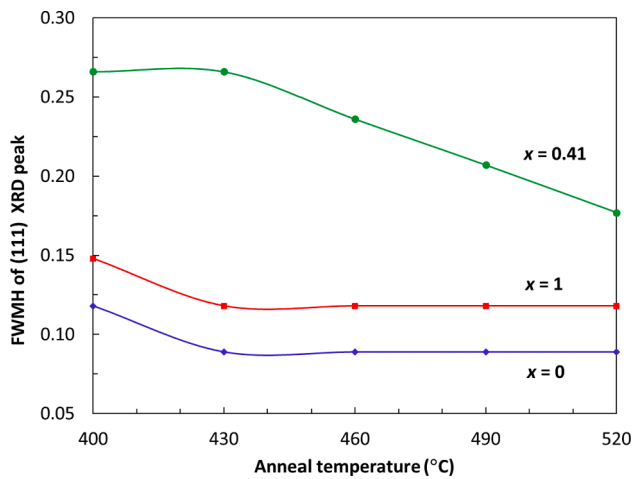**Fig. 9.** FWMH of the (1 1 1) XRD peak with the anneal temperature for selected compositions.

inhomogeneity in the as-deposited $Cd_{1-x}Zn_xTe$ may be greater than the binary films and it reduces substantially upon annealing (provided the mean composition and crystal structure remains unchanged). We did not observe any significant change in the $Cd_{1-x}Zn_xTe$ film composition with annealing (see Table S1 for EDS data measured before and after each anneal temperature).

Further, when the anneal temperature was increased to above 490 °C, there was a relatively greater change in the texture for the $Cd_{1-x}Zn_xTe$ films, in that new reflection peaks emerged, namely (3 1 1) and (4 2 2), whilst intensity of the original peaks, i.e. (1 1 1), (2 2 2), and (5 1 1), decreased (see details in Fig. S3). For CdTe and ZnTe, there was no significant re-orientation observable, apart from lowering in the intensity of (3 1 1) and (4 2 2) reflections in ZnTe, and only the (1 1 1) peak intensity increased on annealing. This is because the chemical stability of these binary alloys is higher than that of the $Cd_{1-x}Zn_xTe$ ternary.

The peak narrowing and re-orientation effects may be attributed to recrystallization and increasing uniformity in the $Cd_{1-x}Zn_xTe$ films. We believe that this results from small variations in alloy composition due to spinodal decomposition [27] during the relatively low growth temperature. Spinodal decomposition relates to segregation effects, to produce two or more stable compounds on a nanometer scale as very finely divided crystalline phases interspersed on a scale of $\sim$ 5–10 nm. Reduction in compositional inhomogeneity suggests higher suitability for the annealed $Cd_{1-x}Zn_xTe$ films as an absorber layer in tandem solar cell application, because grains with higher crystallinity and lower

defect density are expected to reduce the parasitic resistance and improve the photoelectric performance of the device [28].

4. Discussion

The correlation between PL energy and $Cd_{1-x}Zn_xTe$ compositions are mostly reported on low temperature PL spectroscopy and especially for low Zn compositions [10,29–31]. As noted by Zelaya-Angel et al. [32], however, the band bowing parameters of $E_g(x)$ for $Cd_{1-x}Zn_xTe$ do not depend on temperature. In the current work, the compositional dependence of the room temperature PL energy determined for $0 \leq x \leq 1$ is consistent with literature [10]. The fitting parameter, b, from Fig. 4b, also referred to as the bowing parameter, indicates the degree of nonlinearity in the PL energy vs $\times x$ relationship [31]. Reno and Jones [10] reported a bowing parameter of 0.46 from PL characterisation of epitaxial $Cd_{1-x}Zn_xTe$ thin films. This is consistent with the measured b (0.31) from PL spectra in this work. The slight discrepancy between them, however, could be related to differences in film stress (epitaxial vs polycrystalline).

The band bowing parameter obtained from the transmittance and PL spectra are compared in Fig. 10. Also shown is the calculation by Khan et al. [33], which yields $b = 0.68$. Although, the end values (especially at $x \approx 1$) disagree, the curvature of the transmittance (E_g) and calculated data and the value of bowing parameters ($b = 0.70$ derived from transmittance) agree well. Further, Niles and Höchst (1992) reported a value of $b = 0.65$ for their $Cd_{0.8}Zn_{0.2}Te$ sample using photoemission spectroscopy [34]. Although, PL (E_g) data seems to underestimate the value of b, it can also offer an independent metric for determination of the composition in $Cd_{1-x}Zn_xTe$; especially where it is not possible to collect, for example, optical transmittance/absorption from a $Cd_{1-x}Zn_xTe$ layer sandwiched in a multilayer stack (as in tandem solar cells).

During Raman measurements, we noted excitation power density dependent effects, in terms of the spectral features and physical changes to the film appearance. As an exemplar, measurements performed on the CdTe film, using an excitation power density of 3.82×10^4 W/cm^2 with different acquisition times of (I) 5, (II) 25 and (III) 100 s, and a higher power density of 3.82×10^5 W/cm^2 with 5 s acquisition time (IV), are illustrated in Fig. S4. The signal-to-noise ratio of the spectra improves with increasing acquisition time using 3.82×10^4 W/cm^2. No noticeable shifts in the peak position of characteristic phonon modes could be seen from (I) to (III). When the excitation power density was increased by one order of magnitude (3.82×10^5 W/cm^2), both Te-related modes at 123.1 and 141 cm^{-1} are seen to redshift by 5.78 and 2.37 cm^{-1}, respectively, whilst the LO (CdTe) mode smeared out. Optical micrographs taken from the sample surface following the measurements (I) and (IV) indicated that while 3.82×10^4 W/cm^2 excitation (I) does not produce any apparent change to sample surface, following the 3.82×10^5 W/cm^2 irradiation (IV) some damage is observable. According to reports in literature on similarly observed features, the use of high power conditions can produce a Te-enriched region on the II-VI material surface [19,23,25]. This is accompanied with a redshift of the Te-related phonons and smearing out of LO modes of the bulk material.

Several papers also reported the occurrence of Te related Raman modes A_1(Te) and E (Te) at 121 and 141 cm^{-1}, respectively, in related II-VI materials, using high excitation powers. Enhanced intensity of Te specific modes in Raman spectra from CdTe, as a function of excitation power density, has often been explained with surface Te enrichment [19,23], accompanied sometimes with sample surface damage at very high irradiation powers. However, in our work, together with the enhancement in intensity of Te specific phonon modes, we also note interestingly a redshift of both A_1 (Te) and E (Te) peaks with power density (see Fig. 11). The physical process responsible for the production of Te precipitates is still unclear, as the surface temperature rise due to laser heating (estimated to be around 200 K [23]) is insufficient to break chemical bonds and to cause for example Cd evaporation, leaving excess
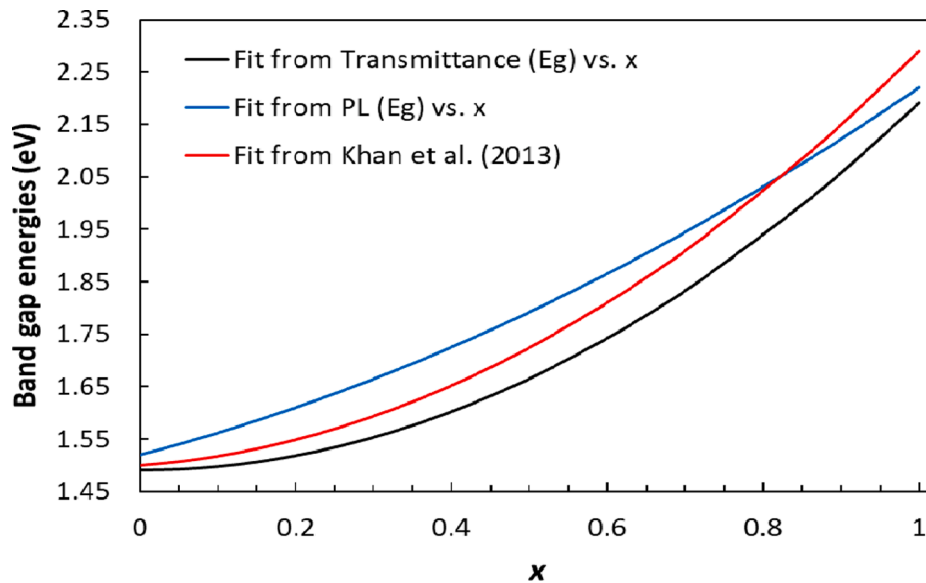
Fig. 10. Band gap energy as a function of composition (x) using fits determined from transmittance (E_g) and PL (E_g) data (present work) and from first-principles calculated data [33].
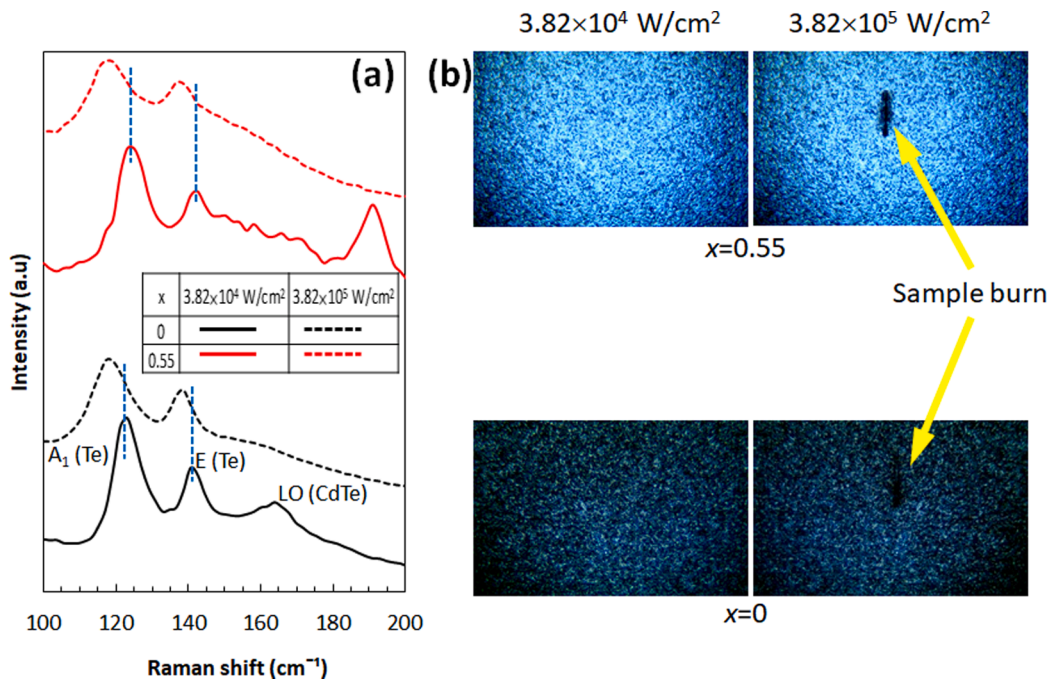

Fig. 11. (a) Comparison of micro-Raman spectra for samples with $x = 0$ and 0.55 recorded with relatively low (3.82×10^4 W/cm^2) and high (3.82×10^5 W/cm^2) laser powers, with 100 and 10 s accumulation times, respectively. (b) Optical micrographs of the samples in (a), following the stated laser exposures.

Te. With one order of magnitude increase in excitation power density, A$_1$ (Te) occurring at 117.32 cm^{-1} is red-shifted by 4.18 cm^{-1} compared to pure Te, which indicates tensile stress [35]. Similar observation is made for the E (Te) mode as well. We note that in the case of an intentional enrichment of Te precipitate density in Cd$_{1-x}$Zn$_x$Te crystals, the Te related Raman modes blue-shifted [36]. For this reason, we attribute the observation of red-shift of Te modes with increasing excitation power to the formation of tensile stress in surface Te. It is clear that optimal measurement conditions are crucial to the reliable measurement and analysis of fundamental Raman features in Cd$_{1-x}$Zn$_x$Te ternary alloys.

Optical micrographs illustrating the physical effect of different irradiation power conditions on sample surface are shown in Fig. S5. No apparent damage was seen on the surface of any of the Cd$_{1-x}$Zn$_x$Te films

following excitations with 3.82×10^4 W/cm^2. However, increasing the power density to 3.82×10^5 W/cm^2 resulted in sample damage, except for ZnTe. This is because the higher excitation power density (3.82×10^5 W/cm^2) must be still below the threshold for sample damage in ZnTe films, which according to Wiedemeier et al. [19] occurs at around 4.4×10^5 W/cm^2, using similar measurement settings as ours. Additionally, we did not observe Te related modes in the Raman spectrum of ZnTe, as this is also characteristic of high-power induced surface damage in ZnTe film [19,37]. This confirms our choice of power settings to collect the PL spectrum of ZnTe (1.91×10^5 W/cm^2), as it appears to be below the threshold of causing surface damage.

We note that the resistivity of our undoped layers is high (Fig. 8). It is anticipated that intentional doping of the Cd$_{1-x}$Zn$_x$Te films will greatly

improve their conductivity; for example, in a previous study, we observed that polycrystalline ZnTe film resistivity can be lowered by 4 orders of magnitude using intentional (arsenic) doping [38]. In addition, due to the work function difference between the electrodes and the $Cd_{1-x}Zn_xTe$ semiconductor, the I-V curve is nonlinear, the photocurrent remains low due to large interface barriers and the resulting high contact resistance. For $x > 0.3$, the barrier at the $ITO/Cd_{1-x}Zn_xTe$ interface must be increasing compared to CdTe, since the illuminated reverse current increases more significantly at these compositions. $Cd_{1-x}Zn_xTe$ and their electrodes can have better ohmic characteristics through intentional doping, enlarging semiconductor grains, work function matching, tailoring of the corresponding preparation process (e.g. contact annealing), or inserting a buffer interlayer [39], and thereby improve the uniformity of electric field inside the device as well as the charge collection rate [28].

5. Conclusion

In this study, physical properties of $Cd_{1-x}Zn_xTe$ thin films ($0 \leq x \leq 1$), prepared at 2 μm thickness on glass substrate in a horizontal MOCVD reactor, were studied in a combinatorial fashion. We found that:

1) For CdTe and at low values of x, the films were rougher with faceted and relatively large grains (0.5–1 μm), and with increasing x up to ZnTe they became smoother with shrinking grain size (~0.1 μm)
2) All films were (1 1 1) out-of-plane textured with $Cd_{1-x}Zn_xTe$ ternary films displaying wider diffraction peaks, interpreted as a sign of larger alloy inhomogeneity due to spinodal decomposition compared to CdTe and ZnTe binaries
3) Compositional dependence of transmittance and photoluminescence varied non-linearly, yielding bowing parameters of 0.70 and 0.31, respectively, which offer independent metrics for the determination of $Cd_{1-x}Zn_xTe$ compositions
4) Raman measurements indicated that (i) ZnTe-like LO mode varies linearly with x (for $x > 0.2$) and hence can also be used to determine the composition of Zn rich films, and (ii) Te-related modes appear and dominate the spectra with increasing excitation power due to surface enrichment of tellurium
5) Electrical resistivity of the films increased by 4 orders of magnitude with increasing x, in tandem with the decreasing grain size towards ZnTe
6) Hydrogen annealing beyond 430 °C reduced the alloy inhomogeneity in the $Cd_{1-x}Zn_xTe$ ternary films, improving their prospect for opto-electronic device applications.

CRediT authorship contribution statement

G. Kartopu: Funding acquisition, Conceptualization, Methodology, Validation, Supervision, Writing - original draft. **Q. Fan:** Investigation, Formal analysis, Writing - review & editing. **O. Oklobia:** Investigation, Formal analysis, Writing - review & editing. **S.J.C. Irvine:** Writing - review & editing.

Declaration of Competing Interest

The authors declared that there is no conflict of interest.

Acknowledgements

Appendix A. Supplementary data

Supplementary data to this article can be found online at https://doi.org/10.1016/j.apsusc.2020.148452.

References

[1] J.P. Mailoa, C.D. Bailie, E.C. Johlin, E.T. Hoke, A.J. Akey, W.H. Nguyen, M.D. McGehee, T. Buonassisi, A 2-terminal perovskite/silicon multijunction solar cell enabled by a silicon tunnel junction, Appl. Phys. Lett. 106 (2015) 121105.
[2] K.A. Bush, A.F. Palmstrom, Z.J. Yu, M. Boccard, R. Cheacharoen, J.P. Mailoa, D.P. McMeekin, R.L.Z. Hoye, C.D. Bailie, T. Leijtens, I.M. Peters, M.C. Minichetti, N. Rolston, R. Prasanna, S. Sofia, D. Harwood, W. Ma, F. Moghadam, H.J. Snaith, T. Buonassisi, Z.C. Holman, S.F. Bent, M.D. McGehee, 23.6%-Efficient Monolithic Perovskite/Silicon Tandem Solar Cells with Improved Stability, Nature Energy 2 (2017) 4.
[3] T. Soga, T. Kato, M. Yang, M. Umeno, T. Jimbo, High efficiency AIGaAs/Si monolithic tandem solar cell grown by metalorganic chemical vapor deposition, J. Appl. Phys. 78 (6) (1995) 4196–4199.
[4] S. Essig, S. Ward, M.A. Steiner, D.J. Friedman, J.F. Geisz, P. Stradins, D.L. Young, Progress towards a 30% efficient GaInP/Si tandem solar cell, Energy Procedia 77 (2015) 464–469.
[5] Oxford PV Perovskite Solar Cell Achieves 28% Efficiency. Available online: https://www.oxfordpv.com/news/oxford-pv-perovskite-solar-cell-achieves-28-efficiency (accessed on 20 April 2020).
[6] S. Essig, M.A. Steiner, C. Allebé, J.F. Geisz, B. Paviet-Salomon, S. Ward, A. Descoeudres, V. LaSalvia, L. Barraud, N. Badel, et al., Realization of GaInP/Si Dual-Junction Solar Cells With 29.8% 1-Sun Efficiency, IEEE J. Photovolt. 6 (2016) 1012–1019.
[7] M. Koç, G. Kartopu, S. Yerci, Combined Optical-Electrical Optimization of $Cd_{1-x}Zn_xTe$/Silicon Tandem Solar Cells, Materials 2020 (1860) 13, https://doi.org/10.3390/ma13081860.
[8] S.D. Sordo, L. Abbene, E. Caroli, A.M. Mancini, A. Zappettini, P. Ubertini, Progress in the Development of CdTe and CdZnTe Semiconductor Radiation Detectors for Astrophysical and Medical Applications, Sensors 9 (2009) 3491–3526, and references therein.
[9] D.J. Olego, P.M. Raccah, J.P. Faurie, Compositional dependence of the Raman frequencies and line shapes of $Cd_{1-x}Zn_xTe$ determined with films grown by molecular-beam epitaxy, Phys. Rev. B 33 (1986) 3819–3822.
[10] J.L. Reno, E.D. Jones, Determination of the dependence of the band-gap energy on composition for $Cd_{1-x}Zn_xTe$, Phys. Rev. B 45 (1992) 1440.
[11] V. Kosyak, Y. Znamenshchykov, A. Cerskus, Y.P. Gnatenko, L. Grase, J. Vecstaudza, A. Medvids, A. Opanasyuk, G. Mezinskis, Composition dependence of structural and optical properties of $Cd_{1-x}Zn_xTe$ thick films obtained by the close-spaced sublimation, J. Alloy. Compd. 682 (2016) 543–551.
[12] S.N. Moger, D.U. Shanubhogue, R. Keshav, M.G. Mahesha, Spectroscopic and electrical analysis of vacuum co-evaporated $Cd_xZn_{1-x}Te$ thin films, Superlattices Microstruct. 142 (2020), 106521.
[13] G. Kartopu, S. Irvine (2020). Cadmium Telluride and Related II-VI Materials. In Metalorganic Vapor Phase Epitaxy (MOVPE) (eds S. Irvine and P. Capper). doi: 10.1002/9781119313021.ch10.
[14] J. Camacho, A. Cantarero, Raman spectroscopy and photoluminescence of ZnTe thin films grown on GaAs, J. Appl. Phys. 92 (2002) 6014.
[15] G. Kartopu, S.C. Bayliss, R.E. Hummel, Y. Ekinci, Simultaneous micro-Raman and photoluminescence study of spark-processed germanium: Report on the origin of the orange photoluminescence emission band, J. Appl. Phys. 95 (2004) 3466.
[16] P.M. Amirtharaj, F.H. Pollak, Raman scattering study of the properties and removal of excess Te on CdTe surfaces, Appl. Phys. Lett. 45 (1984) 789.
[17] X. Wu, J. Yu, T. Ren, L. Liu, Micro-Raman spectroscopy measurement of stress in silicon, Microelectron. J. 38 (2007) 87–90.
[18] S.L. Lopez, G.T. Delgado, S.J. Sandoval, O.J. Sandoval, R.C. Perez, M.M. Lira, Structure and electronic properties of the novel semiconductor alloy $Cd_{1-x}Cu_xTe$, J. Vac. Sci. Technol., A 17 (1999) 1958.
[19] V. Wiedemeier, G. Berth, A. Zrenner, E.M. Larramendi, U. Woggon, K. Lischka, D. Schikora, In situ characterization of ZnTe epilayer irradiation via time-resolved and power-density-dependent Raman spectroscopy, Semicond. Sci. Technol. 26 (2011), 105023.
[20] Y.V. Znamenshchykov, V.V. Kosyak, A.S. Opanasyuk, V.O. Dorda, P.M. Fochuk, A. Medvids, Raman Characterisation of $Cd_{1-x}Zn_xTe$ Thick Polycrystalline Films Obtained by the Close-Spaced Sublimation, Acta Phys. Pol. A 132 (2017).
[21] D.N. Talwar, Z.C. Feng, P. Becla, Impurity-induced phonon disordering in $Cd_{1-x}Zn_xTe$ ternary alloys, Phys. Rev. B 48 (1993) 17064.
[22] A. Aydinli, A. Compaan, G. Contreras-Puente, A. Mason, Polycrystalline $Cd_{1-x}Zn_xTe$ thin films on glass by pulsed laser deposition, Solid State Commun. 8 (7) (1991) 465–468.
[23] M.J. Soares, J.C. Lopes, M.C. Carmo, A. Neves, Micro-Raman Study of laser damage in CdTe, Physica Status Solidi (c) 1 (2) (2004) 278–289.
[24] S. Perkowitz, L.S. Kim, Z.C. Feng, Optical phonons in $Cd_{1-x}Zn_xTe$, Physical Review B 42 (2) (1990) 1455–1457.
[25] S.A. Hawkins, E. Villa-Aleman, M.C. Duff, D.B. Hunter, A. Burger, M. Groza, V. Buliga, D.R. Black, Light-Induced Tellurium Enrichment on CdZnTe Crystal

Surfaces Detected by Raman Spectroscopy, J. Electron. Mater. 37 (9) (2008) 1438–1443.

[26] S.M. Sze, Physics of Semiconductor Devices, Wiley, New York, 1983, p. 88.

[27] S.M. Allen, in Encyclopedia of Materials: Science and Technology, DOI: 10.1016/B0-08-043152-6/01569-2, 2001.

[28] S. Chander, M. S. Dhaka, Thermal annealing induced physical properties of electron beam vacuum evaporated CdZnTe thin films. Thin Solid Films 625 (2017) 13-137; S. Chandera, A.K. Dea, M.S. Dhakab, Towards CdZnTe solar cells: An evolution to post-treatment annealing atmosphere. Solar Energy 174 (2018) 757–761.

[29] W.M. Duncan, R.J. Koestner, J.H. Tregilgas, H.-Y. Liu, M.-C. Chen, Nondestructive compositional and defect characterisation of CdZnTe alloys using photoluminescence spectroscopy, Materials Science Society Symposium Proceedings 161 (1990).

[30] S.P. Tobin, J.P. Tower, D. Chandler-Horowitz, P.M. Amirtharaj, V.C. Lopes, W. M. Duncan, A.J. Syllaios, C.K. Árd, N.C. Giles, J. Lee, R. Balasubramanian, A. B. Bollong, T.W. Steeiner, M.L.W. Thewalt, D.K. Bowen, B.K. Tanner, A comparison of techniques for nondestructive composition measurements in CdZnTe substrates, J. Electron. Mater. 24 (5) (1995).

[31] J.E. Toney, B.A. Brunett, T.E. Schlesinger, J.M. Van Scyoc, R.B. James, M. Schieber, M. Goorsky, H. Yoon, E. Eissler, C. Johnson, Uniformity of $Cd_{1-x}Zn_xTe$ grown by high-pressure Bridgman, Nuclear Instruments and Methods in Physics Research A 380 (1996) 132–135.

[32] O. Zelaya-Angel, J.G. Mendoza-Alvarez, M. Becerril, On the bowing parameter in $Cd_{1-x}Zn_xTe$, J. Appl. Phys. 95 (2004) 6284.

[33] I. Khan, H.A. Rahnamaye, W. Aliabad, Z. Ahmad, I. Ahmad Ali, First principle optoelectronic studies of visible light sensitive CZT, Superlattices Microstruct. 63 (2013) 91–99.

[34] D. W. Niles, H. Höchst, Determination of the bowing parameter of the split-off band in Cd0.8Zn0.2Te (100) by angle-resolved photoemission spectroscopy. Physical Review B, 46 (3), 1992.

[35] Xu. Zongwei, Zhongdu He, Ying Song, Fu. Xiu, Mathias Rommel, Xichun Luo, Alexander Hartmaier, Junjie Zhang, Fengzhou Fang, Topic Review: Application of Raman Spectroscopy Characterization in Micro/Nano-machining, Micromachines 9 (2018) 361, https://doi.org/10.3390/mi9070361.

[36] J. Min, X. Liang, J. Chen, D. Wang, H. Li, J. Zhang, Investigations of Te inclusions in CdZnTe crystalline material using Raman spectroscopy and IR techniques, Vacuum 86 (2012) 1003–1006.

[37] E.M. Larramendi, G. Berth, V. Wiedemeier, K.-P. Hüsch, A. Zrenner, U. Woggon, E. Tschumak, K. Lischka, D. Schikora, Intensity enhancement of Te Raman modes by laser damage in ZnTe epilayers, Semicond. Sci. Technol. 25 (2010), 075003.

[38] O. Oklobia, G. Kartopu, S.J.C. Irvine, Properties of Arsenic-Doped ZnTe Thin Films as a Back Contact for CdTe Solar Cells, Materials 12 (2019) 3706, https://doi.org/10.3390/ma12223706.

[39] Y. Shen, J. Huang, Q. Gu, H. Meng, K. Tang, Y. Shen, J. Zhang, L. Wang, Y. Lu, The investigation of Ga-doped ZnO as an interlayer for ohmic contact to $Cd_{1-x}Zn_xTe$ films, Appl. Surf. Sci. 425 (2017) 176–179.